

# Digital quantum simulation of NMR experiments

Kushal Seetharam\*,<sup>1,2</sup> Debopriyo Biswas,<sup>3,4</sup> Crystal Noel,<sup>3,4</sup> Andrew Risinger,<sup>4</sup> Daiwei Zhu,<sup>4</sup> Or Katz,<sup>3</sup> Sambuddha Chattopadhyay,<sup>2</sup> Marko Cetina,<sup>4,5</sup> Christopher Monroe,<sup>3,4,6</sup> Eugene Demler,<sup>7</sup> and Dries Sels<sup>8,9</sup>

<sup>1</sup>*Department of Electrical Engineering, Massachusetts Institute of Technology, Cambridge, Massachusetts 02139, USA*

<sup>2</sup>*Department of Physics, Harvard University, Cambridge, MA, 02138, USA*

<sup>3</sup>*Department of Electrical and Computer Engineering, Department of Physics, Duke Quantum Center, Duke University, Durham, North Carolina 27708, USA*

<sup>4</sup>*Joint Quantum Institute, Department of Physics, University of Maryland, College Park, Maryland 20742, USA*

<sup>5</sup>*Department of Physics, Duke Quantum Center, Duke University, Durham, North Carolina 27708, USA*

<sup>6</sup>*IonQ, Inc., College Park, Maryland 20740, USA*

<sup>7</sup>*Institute for Theoretical Physics, ETH Zürich, 8093 Zürich, Switzerland*

<sup>8</sup>*Department of Physics, New York University, New York, NY, 10003, USA*

<sup>9</sup>*Center for Computational Quantum Physics, Flatiron Institute, New York, NY, 10010, USA*

Computational simulations of nuclear magnetic resonance (NMR) experiments are essential for extracting information about molecular structure and dynamics, but are often intractable on classical computers for large molecules such as proteins and protocols such as zero-field NMR. We demonstrate the first quantum simulation of a NMR spectrum, computing the zero-field spectrum of the methyl group of acetonitrile on a trapped-ion quantum computer. We reduce the sampling cost of the quantum simulation by an order of magnitude using compressed sensing techniques. Our work opens a new practical application for quantum computation, and we show how the inherent decoherence of NMR systems may enable the simulation of classically hard molecules on near-term quantum hardware.

Nuclear magnetic resonance (NMR) spectroscopy is a widely used tool in materials chemistry and structural biology, providing insight into the structure, conformational dynamics, reaction state, and chemical environment of molecules [1]. For example, NMR is employed to probe the structure of promising photovoltaic candidates [2] as well as medically-relevant biomolecules such as the intrinsically disordered proteins that cause Alzheimer’s and Parkinson’s [3, 4]. Despite their versatility, NMR experiments can be difficult to interpret, often requiring numerical simulation of the molecule’s nuclear spin dynamics [3, 5]. The spin correlations in these quantum systems can spread in an exponentially large state space, making simulation on classical computers intractable for large molecules as well as for emerging experimental protocols such as zero-field NMR [6, 7]. Quantum computers and simulators, however, are well-positioned to simulate the dynamics of spin systems [8]; such simulations may be the first practical application of quantum computers to achieve a speed-up compared to classical computers [9].

Here, we simulate a zero-field NMR experiment on a trapped-ion quantum computer [10]. The quantum computer implements a sequence of unitary rotations and entangling interactions on  $^{171}\text{Yb}^+$  ion qubits to implement the quantum circuit that emulates the NMR experiment [11]. We specifically compute the spectrum of acetonitrile, a solvent with four NMR-active nuclear spins, and show that the resonance frequencies in the spectrum quantitatively match the experimental NMR data from Ref. [12]. We obtain high spectral resolution within the resource limitations of the trapped-ion device by exploit-

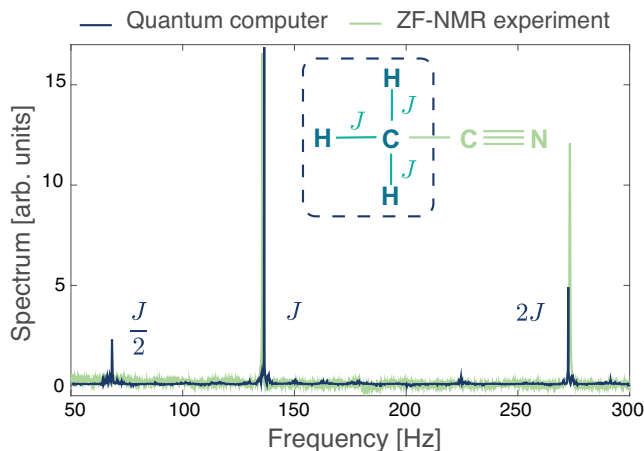


Figure 1: Zero-field spectrum of acetonitrile computed on an ion-trap quantum computer compared with the NMR experiment performed in Ref. [12]. The inset shows the chemical structure of acetonitrile, highlighting the methyl group that was probed in the experiment.

ing compressed sensing techniques [13] and a state-of-the-art quantum circuit synthesis algorithm [14]. These techniques can be used to reduce the resource cost of simulating classically hard NMR systems, and are likely to prove useful in quantum simulations of hard systems that appear in quantum chemistry and condensed matter physics [15]. We give resource estimates for quantum simulations of hard NMR systems, showing how the dephasing inherent in nuclear spin dynamics may enable such simulations on near-term quantum hardware.

A NMR experiment involves polarizing the nuclear spins of a molecular sample via an external magnetic field or a chemical process, letting the spins evolve in time, and then measuring the average magnetization of the system. The measured time-dependent magnetization is called the free induction decay (FID), and its Fourier transform yields the NMR spectrum. Letting the operators  $\{\mathbf{S}_i\}$  represent the nuclear spins, the initial polarized state of the system can be described as  $\rho_0 \propto \tilde{S}_{\text{tot}}^z$ , where  $\tilde{S}_{\text{tot}}^z = \sum_i \gamma_i S_i^z$  and  $\gamma_i$  is the gyromagnetic ratio of the nuclear isotope  $i$  relative to that of a proton. In the case of a 1D NMR experiment, the measured FID corresponds to the quantity

$$\text{FID}(t) = \text{Tr} \left[ U(t)^\dagger \tilde{S}_{\text{tot}}^z U(t) \tilde{S}_{\text{tot}}^z \right], \quad (1)$$

where  $U(t) = \exp(-iHt/\hbar)$  produces the time-evolution of the system generated by a Hamiltonian  $H$ . The evolution of liquid-state molecular samples is typically well captured by

$$H = \sum_{i,j} J_{ij} \mathbf{S}_i \cdot \mathbf{S}_j + \sum_i h_i S_i^x, \quad (2)$$

where we have taken Planck's constant  $\hbar = 1$ . The  $J$ -couplings  $\{J_{ij}\}$  characterize the strength of bond-mediated exchange interactions and the chemical shifts  $\{h_i\}$  represent local magnetic screening around nuclei in different chemical environments in response to an external magnetic field [1].

Zero-field NMR protocols avoid the external field, opening the possibility of portable and cheaper experiments as they obviate the need for cryogenically cooled superconducting magnets. The resulting spectra can have narrower resonance lines than conventional high-field NMR due to high absolute field homogeneity and stability [6, 7, 12], and may enable the study of nanoscale samples [16–18]. Without a large background field, however, the interactions between spins become dominant. Therefore, a significant limitation of zero-field protocols is that their spectra are hard to interpret without access to reliable computational simulations of the NMR experiment, which can be rendered classically intractable for even intermediate scale molecules [19].

We compute the zero-field spectrum of acetonitrile, a compound which is commonly used as an industrial solvent. The molecule has four NMR-active nuclear spins, a  $^{13}\text{C}$  and three  $^1\text{H}$ , that make up a methyl group (see inset in Fig. 1). There are three non-zero  $J$ -couplings, corresponding to the three  $^{13}\text{C}$ – $^1\text{H}$  bonds, all with value  $J = 136.2$  Hz. The FID signal of Eq. (1) can be computed on a quantum computer by initializing the system qubits in computational basis states with a positive average magnetization, enacting time-evolution under the Hamiltonian via an appropriate quantum circuit, Eq. (2), and then measuring the average magnetization of the system. We write this measurable as

$$\text{FID}(t) = \sum_{\tilde{m}_n > 0} \tilde{m}_n \langle \tilde{m}_n(t) | \tilde{S}_{\text{tot}}^z | \tilde{m}_n(t) \rangle, \quad (3)$$

where  $\{|\tilde{m}_n\rangle; \tilde{m}_n\}$  are the eigenstates and eigenvalues of  $\tilde{S}_{\text{tot}}^z$ , and  $|\tilde{m}_n(t)\rangle = U(t)|\tilde{m}_n\rangle$ . For a system of  $N$  spins, the sum in Eq. (3) can have a number of terms that scales exponentially with  $N$ , potentially negating any quantum computational advantage. The sampling cost can, however, be reduced to  $N^2$  via importance sampling and thus the advantage is preserved [8].

Figure 1 shows the spectrum we compute on an ion trap quantum computer in comparison with the seminal zero-field NMR experiment of Ref. [12]. We see that the quantum computation accurately reproduces the resonances at frequencies  $J$  and  $2J$ . Specifically, the corresponding resonance frequencies extracted from the quantum simulation are  $136.20 \pm 0.09$  Hz and  $272.41 \pm 0.09$  Hz, which are within  $1\sigma$  of the exact frequencies of 136.2 Hz and 272.4 Hz. The extracted resonance frequency uncertainty is Fourier limited; a Lorentzian fit to the reconstructed peaks results in a width smaller than the frequency grid spacing. We therefore take half the grid spacing as the uncertainty. Given that the zero-field NMR experiment can only resolve the spectral peaks within 0.1 Hz [12], we demonstrate that quantum computers can simulate NMR experiments within their resolution.

The spectrum computed on the quantum computer exhibits an additional resonance at  $J/2$  that is not present in the NMR experiment. This additional spectral peak arises from a combination of errors in the quantum computer and the high-symmetry of the molecule, which induces dynamical recurrences that are captured by the specific method we use to synthesize the time-evolution circuits. Such artifacts are unlikely to appear in classically intractable NMR simulations whose large, strongly correlated molecules typically do not exhibit dynamical recurrences. Furthermore, we provide a simple method to remove artifact peaks in future experiments even for the small, highly symmetric systems where they may occur [11].

In order to calculate the spectrum, we first compute the FID, Eq. (3), at a non-uniform random sampling of time points lower than the Nyquist rate. We synthesize the time-evolution quantum circuits using the numerical optimization algorithm in Ref. [14] after tailoring it to the gate set and qubit topology of the trapped ion device [11]. This numerical synthesis procedure efficiently produces low-depth circuits but is limited to a small number qubits. It can, however, be a useful tool when simulating larger systems [11].

The undersampled FID measured in experiment is reconstructed into a spectrum by a recovery algorithm which assumes that the time domain signal is sparse in the frequency domain. These two steps – non-uniform sampling (NUS) and spectral reconstruction – form the basis of compressed sensing. Compressed sensing techniques have their root in information theory [21], but have been further developed in the experimental NMR community where they can drastically reduce the data collection burden [13]. While these techniques have recently been used in quantum sensing [22], we demon-

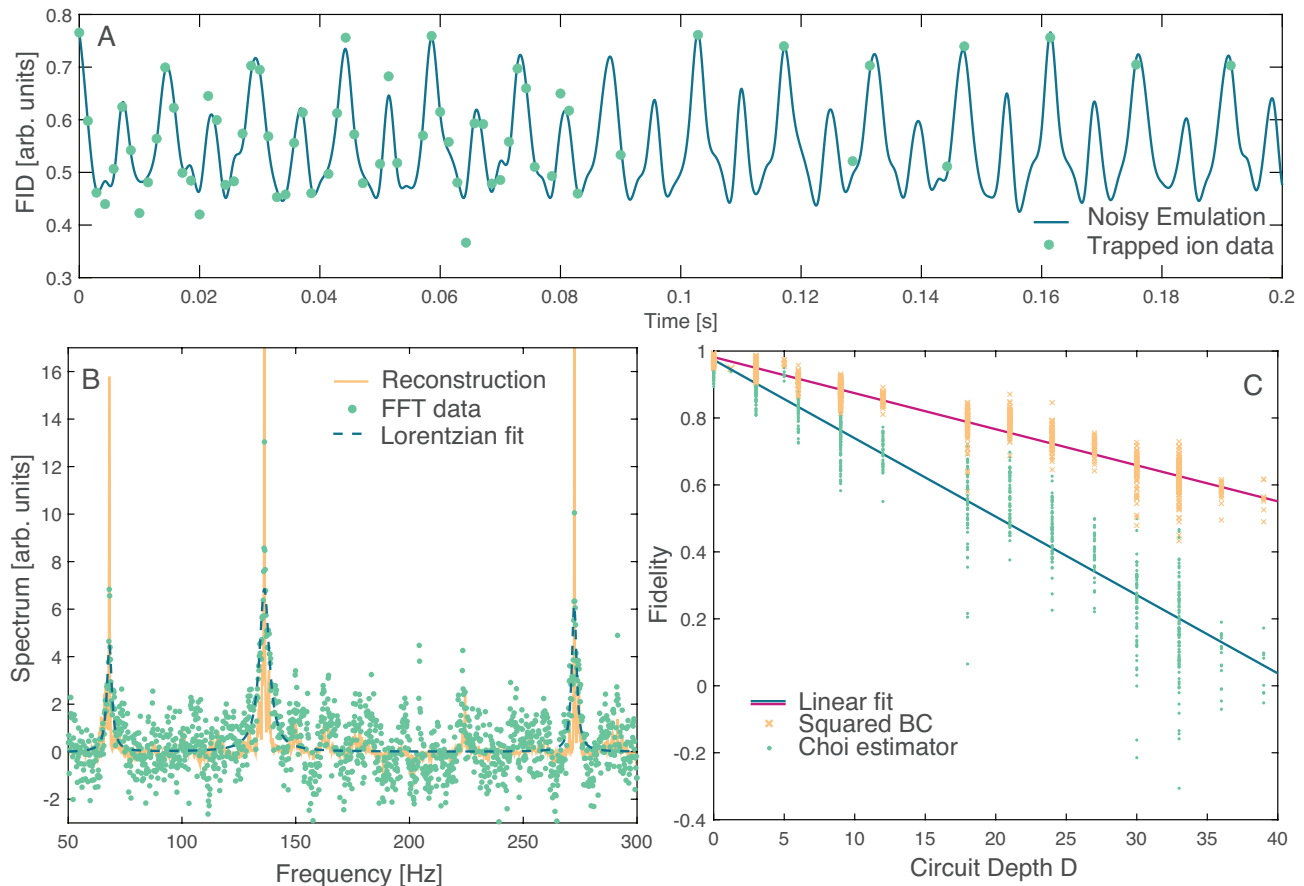


Figure 2: **Compressed sensing reconstruction & Benchmarking.** **A** Comparison of the FID of a noisy quantum circuit emulation (blue line) and the non-uniform, and sparsely sampled, experimentally measured point (green circles). The noise is modeled by two-qubit gates subject to both amplitude and phase damping with rates 0.005 and 0.035 respectively. **B** NMR spectrum extracted from the digital quantum simulation. Green dots show the Fourier transform of the FID after replacing unsampled points with zeros. Dashed blue line shows the best (under  $\ell_1$ -norm) Lorentzian fits to the zero-padded data. Solid yellow line shows the reconstructed spectrum after applying the IST-S algorithm. The y-axis is rescaled (zoomed-in) compared to Fig. 1 to make the features more visible. **C** Fidelity of quantum simulation. The yellow crosses show the squared Bhattacharyya coefficient and the green dots show a fidelity estimator recently introduced by Choi et al. [20] as a function of the circuit depth measured in the number of two-qubit gates.

strate their use in quantum simulation experiments to similarly reduce the computational cost [15]. In Fig. 2A we plot a noisy emulation of the ion trap experiment at all values of the uniform dense time grid and compare to the NUS points that were actually collected in the experiment. Experimental data was collected up to times  $t = 6$  [11], but is only shown up to  $t = 0.2$  to allow a clear comparison to the noisy emulation. We use a sine-weighted Poisson gap NUS schedule that is dense at short times as it has been shown to reduce reconstruction artifacts [23]. Figure 2B shows the spectrum resulting from Fourier transforming the experimental data before running the reconstruction algorithm. We see that the signal-to-noise ratio in this raw spectrum is poor due to NUS artifacts, with a Lorentzian fit to the peaks resulting in an uncertainty of approximately 1 Hz. The same spec-

trum is shown after we run the iterative soft thresholding (IST-S) reconstruction algorithm; the signal-to-noise is dramatically improved, with the uncertainty reducing by an order of magnitude to approximately 0.1 Hz. The reconstructed spectrum matches the spectrum resulting from fully sampled noisy emulation [11]. Experimentally, only 102 out of the 4096 time points were collected, indicating that compressed sensing reduced the computational burden of the experiment by more than a factor of 40. This reduction is particularly crucial for experiments with slow repetition rates.

In Fig. 2C, we assess the quality of the trapped-ion simulation by comparing the outputs of all 102 circuits ( $\times 8$  initial states) with the ideal outputs resulting from a noiseless circuit emulation. The Bhattacharyya coefficient, which provides an upper bound for the fidelity

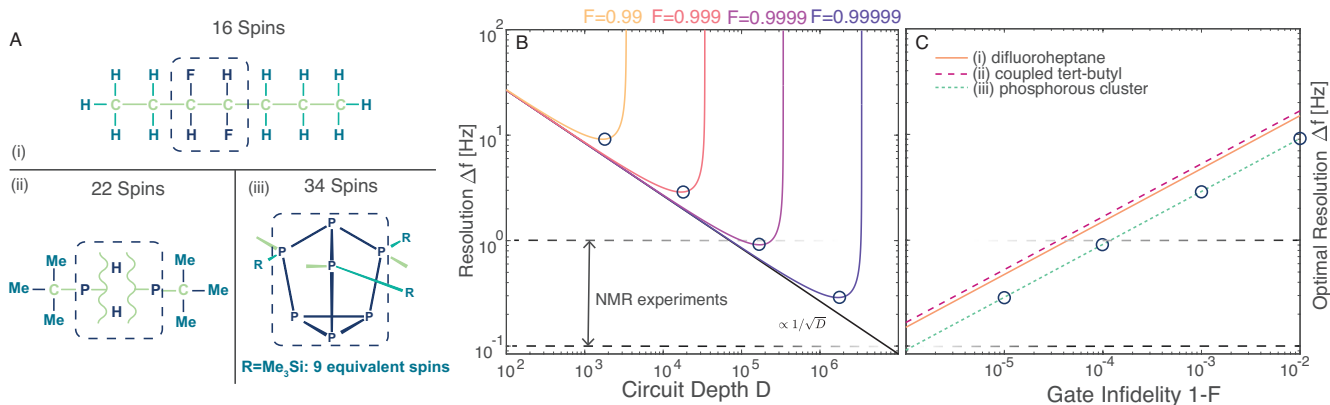


Figure 3: **Scaling up to classically hard simulations.** **A** Chemical structures of (i) anti-3,4-difluoroheptane (ii) a system with two coupled tert-butyl groups and (iii) the B[ACR<sub>9</sub>]<sub>3</sub> phosphorous system. Light green atoms do not contribute to the NMR signal and dashed boxes indicate strongly interacting clusters whose circuit synthesis can significantly speed up the quantum computation [11]. **B** Experimental design curves for (Me<sub>3</sub>Si)<sub>3</sub>P<sub>7</sub> (panel A(iii)), showing  $1/\sqrt{D}$  scaling, where  $D$  is the circuit depth, of the frequency resolution up to a minimally achievable width set by the decoherence of the quantum computer. The circuit depth is measured by the number of fully-connected two-qubit gates. **C** Optimal resolution for all three molecules. The circles indicate the resolution at optimal circuit depth and the dashed black horizontal lines indicate the resolution accessible in NMR experiments.

of the prepared quantum state [11], indicates that a typical two-qubit gate operation was enacted with fidelity at most 98.9%. We also examine the fidelity estimator of Ref. [20], which yields an estimate of 97.7% fidelity per operation.

While the present experiment is performed on state-of-the-art quantum hardware, it is still easily tractable on a classical computer. In order to elucidate the hardware resources required to scale quantum simulations to classically hard NMR experiments, we examine three challenging systems that are at the border of what is classically simulable. The compounds are depicted in Fig. 3A. Each system can be classically simulated using Spinach [24], an advanced classical simulation package, in several hours, provided access to 32 CPU cores, 128 GB RAM, and a graphics card as powerful as the Titan V. The interaction graphs characterizing the molecules' nuclear spin Hamiltonians have a compact structure, and are composed of strongly interacting clusters of four to seven spins which are weakly connected to other clusters. The compact nature of the interaction graphs—which give rise to rapidly spreading strong correlations—makes these systems hard to classically simulate, even though these NMR experiments can be described without the long-range dipolar interactions that are central to other challenging NMR protocols.

We estimate the resources required to simulate these systems using a quantum computer by using product formulas to prescribe circuits that implement time-evolution under the Hamiltonian of Eq. (2). While there are many quantum algorithms that implement quantum dynamics, product formulas are considered to have the lowest resource overhead and be most suitable for early quantum devices [9, 25]. We exploit both the cluster structure of

the nuclear interactions as well as inherent dephasing in the NMR experiment to further reduce the cost [11].

In Fig. 3B, we plot the achievable linewidth,  $\Delta f$ , of the NMR spectrum as a function of the circuit depth  $D$  for quantum computers with various levels of decoherence, using a clustered first order product formula. We define the circuit depth as the number of fully-connected two-qubit gates, as available in ion trap quantum computers [10]. We observe a  $1/\sqrt{D}$  scaling, reminiscent of the standard quantum limit, up to a critical depth where the decoherence of the quantum computer takes over. At any given value of the gate fidelity  $F$  there is an optimal circuit depth  $\sim 1/\log(1/F)$  arising from a competition between algorithmic error and decoherence, resulting in linewidth  $\Delta f \sim \sqrt{\log(1/F)}$ . Fig. 3C depicts the expected optimal linewidth for all the molecules considered in this work. While we clearly observe that the larger molecules from Fig. 3A are considerably harder to simulate than the four spin methyl group that was computed here, it should be noted that these curves are expected to saturate for Hamiltonians corresponding to clustered molecules. To simulate the phosphorus cluster (Fig. 3A(iii)) to the same level as the physical NMR experiment, we expect to require circuits of  $O(10^5)$  gates with a typical gate infidelity of  $O(10^{-4})$ , an infidelity that is two orders of magnitude better than the present experiment. Such infidelities have been achieved in small trapped-ion systems [26, 27], and future scaling strategies hold great promise for reaching the above performance metrics [28].

Our demonstration provides the first proof of principle that quantum computers can simulate NMR spectra within experimental resolution. Simulations of NMR experiments on quantum hardware would not only be in-

valuable to analyzing conventional NMR experiments in systems consisting of hundreds to thousands of spins [5] but could also help realize the full potential of emerging modalities that explore strong spin-correlations such as zero-field, low-field, and nanoscale NMR. These latter protocols generate spectra that are especially difficult to interpret without computational simulations, which in turn can prove classically intractable for systems of even a few tens of spins [29].

While scaling quantum NMR simulations to classically intractable systems will be challenging, it should be noted that the resource projections in Fig. 3 are significantly less demanding than most other near-term quantum computing applications [9, 30, 31]. The physical reason behind the reduced resource cost is that dephasing is inherent in the dynamics of nuclear spin systems, with a rate given by the finite line-width of spectral peaks in NMR experiments. Quantum simulations can tolerate decoherence in the quantum device as long as it is less than the dephasing rate of the spin system [8]. NMR thus provides a natural task where we can seek a practical quantum advantage from near-term quantum devices: simulation of noisy spin systems using noisy quantum computers.

## ACKNOWLEDGEMENTS

We thank Ilya Kuprov, Haribabu Arthanari, and Minh Tran for stimulating discussions. K.S. and E.D. acknowledge funding from ARO grant number W911NF-20-1-0163, Harvard-MIT CUA, NSF EAGER-QAC-QCH award No. 2037687, and the NSF grant No. OAC-1934714. DB, CN, AR, DZ, OK, MC, and CM acknowledge support by the ARO through the IARPA LogiQ program (11IARPA1008), the NSF STAQ Program (PHY-1818914), the AFOSR MURIs on Dissipation Engineering in Open Quantum Systems (FA9550-19-1-0399) and Quantum Interactive Protocols for Quantum Computation (FA9550-18-1-0161), the ARO MURI on Modular Quantum Circuits (W911NF1610349), and the U.S. Department of Energy Quantum Systems Accelerator (QSA) Research Center (DE-FOA-0002253). S.C. acknowledges funding from the NSF GRFP. D.S. acknowledges funding from the Harvard Quantum Initiative Seed Funding program and AFOSR: Grant FA9550-21-1-0236. The Flatiron Institute is a division of the Simons Foundation.

- 
- [1] M. H. Levitt, *Spin Dynamics: Basics of Nuclear Magnetic Resonance* (John Wiley & Sons Ltd, 2008).
- [2] D. J. Kubicki, S. D. Stranks, C. P. Grey, and L. Emsley, *Nature Reviews Chemistry* **5**, 624 (2021).
- [3] B. Reif, S. E. Ashbrook, L. Emsley, and M. Hong, *Nature Reviews Methods Primers* **1**, 2 (2021).
- [4] H. J. Dyson and P. E. Wright, *Current Opinion in Structural Biology* **70**, 44 (2021).
- [5] L. J. Edwards, D. Savostyanov, Z. Welderufael, D. Lee, and I. Kuprov, *Journal of Magnetic Resonance* **243**, 107 (2014).
- [6] T. Theis, P. Ganssle, G. Kervern, S. Knappe, J. Kitching, M. P. Ledbetter, D. Budker, and A. Pines, *Nature Physics* **7**, 571 (2011).
- [7] D. A. Barskiy, M. C. D. Tayler, I. Marco-Rius, J. Kurhanewicz, D. B. Vigneron, S. Cikriki, A. Aydogdu, M. Reh, A. N. Pravdivtsev, J.-B. Hövener, J. W. Blanchard, T. Wu, D. Budker, and A. Pines, *Nature Communications* **10**, 3002 (2019).
- [8] D. Sels, H. Dashti, S. Mora, O. Demler, and E. Demler, *Nature Machine Intelligence* **2**, 396 (2020).
- [9] A. M. Childs, D. Maslov, Y. Nam, N. J. Ross, and Y. Su, *Proceedings of the National Academy of Sciences* **115**, 9456 (2018), <https://www.pnas.org/content/115/38/9456.full.pdf>.
- [10] L. Egan, D. M. Debroy, C. Noel, A. Risinger, D. Zhu, D. Biswas, M. Newman, M. Li, K. R. Brown, M. Cetina, and C. Monroe, “Fault-tolerant operation of a quantum error-correction code,” (2020), arXiv:2009.11482 [quant-ph].
- [11] See supplementary materials.
- [12] M. P. Ledbetter, T. Theis, J. W. Blanchard, H. Ring, P. Ganssle, S. Appelt, B. Blümich, A. Pines, and D. Budker, *Phys. Rev. Lett.* **107**, 107601 (2011).
- [13] M. Bostock and D. Nietlispach, *Concepts in Magnetic Resonance Part A* **46A** (2017), 10.1002/cmr.a.21438.
- [14] E. Younis, K. Sen, K. Yelick, and C. Iancu, “Qfast: Conflating search and numerical optimization for scalable quantum circuit synthesis,” (2021), arXiv:2103.07093 [quant-ph].
- [15] X. Andrade, J. N. Sanders, and A. Aspuru-Guzik, *Proceedings of the National Academy of Sciences* **109**, 13928 (2012), <https://www.pnas.org/content/109/35/13928.full.pdf>.
- [16] H. J. Mamin, M. Kim, M. H. Sherwood, C. T. Rettner, K. Ohno, D. D. Awschalom, and D. Rugar, *Science* **339**, 557 (2013), <https://science.sciencemag.org/content/339/6119/557.full.pdf>.
- [17] T. Staudacher, F. Shi, S. Pezzagna, J. Meijer, J. Du, C. A. Meriles, F. Reinhard, and J. Wrachtrup, *Science* **339**, 561 (2013), <https://science.sciencemag.org/content/339/6119/561.full.pdf>.
- [18] I. Lovchinsky, A. O. Sushkov, E. Urbach, N. P. de Leon, S. Choi, K. De Greve, R. Evans, R. Gertner, E. Bersin, C. Müller, L. McGuinness, F. Jelezko, R. L. Walsworth, H. Park, and M. D. Lukin, *Science* **351**, 836 (2016), <https://science.sciencemag.org/content/351/6275/836.full.pdf>.
- [19] T. E. O’Brien, L. B. Ioffe, Y. Su, D. Fushman, H. Neven, R. Babbush, and V. Smelyanskiy, “Quantum computation of molecular structure using data from challenging-to-classically-simulate nuclear magnetic resonance experiments,” (2021), arXiv:2109.02163 [quant-ph].
- [20] J. Choi, A. L. Shaw, I. S. Madjarov, X. Xie, J. P. Covey, J. S. Cotler, D. K. Mark, H.-Y. Huang, A. Kale, H. Pichler, F. G. S. L. Brandão, S. Choi, and M. Endres, “Emergent randomness and benchmarking from many-body quantum chaos,” (2021), arXiv:2103.03535 [quant-ph].

- [21] D. Donoho, IEEE Transactions on Information Theory **52**, 1289 (2006).
- [22] K. Arai, C. Belthangady, H. Zhang, N. Bar-Gill, S. J. Devience, P. Cappellaro, A. Yacoby, and R. L. Walsworth, Nature Nanotechnology **10**, 859 (2015).
- [23] S. G. Hyberts, K. Takeuchi, and G. Wagner, Journal of the American Chemical Society **132**, 2145 (2010), pMID: 20121194, <https://doi.org/10.1021/ja908004w>.
- [24] H. Hogben, M. Krzystyniak, G. Charnock, P. Hore, and I. Kuprov, Journal of Magnetic Resonance **208**, 179 (2011).
- [25] A. M. Childs, Y. Su, M. C. Tran, N. Wiebe, and S. Zhu, Phys. Rev. X **11**, 011020 (2021).
- [26] J. Gaebler, Ting, Y. Wan, Y. Lin, R. Bowler, A. Keith, S. Glancy, K. Coakley, E. Knill, D. Leibfried, and D. Wineland, (2016).
- [27] C. J. Ballance, T. P. Harty, N. M. Linke, M. A. Sepiol, and D. M. Lucas, Phys. Rev. Lett. **117**, 060504 (2016).
- [28] K. R. Brown, J. Kim, and C. Monroe, npj Quantum Information **2**, 16034 (2016).
- [29] J. R. McClean, N. C. Rubin, J. Lee, M. P. Harrigan, T. E. O'Brien, R. Babbush, W. J. Huggins, and H.-Y. Huang, "What the foundations of quantum computer science teach us about chemistry," (2021), arXiv:2106.03997 [quant-ph].
- [30] M. Kühn, S. Zanker, P. Deglmann, M. Marthaler, and H. Weib, Journal of Chemical Theory and Computation **15**, 4764 (2019).
- [31] J. F. Gonthier, M. D. Radin, C. Buda, E. J. Duskocil, C. M. Abuan, and J. Romero, "Identifying challenges towards practical quantum advantage through resource estimation: the measurement roadblock in the variational quantum eigensolver," (2020), arXiv:2012.04001 [quant-ph].
- [32] J. T. Merrill and K. R. Brown, "Progress in compensating pulse sequences for quantum computation," in *Quantum Information and Computation for Chemistry* (John Wiley & Sons, Ltd, 2014) pp. 241–294.
- [33] K. Mølmer and A. Sørensen, Phys. Rev. Lett. **82**, 1835 (1999).

# SUPPLEMENTAL MATERIALS FOR DIGITAL QUANTUM SIMULATION OF NMR EXPERIMENTS

## S1. METHODS

### A. Data collection

NMR simulation circuits are run on a trapped ion quantum computer that uses the  $^2S_{1/2}$  states of  $^{171}\text{Yb}^+$  ions as the qubit states. We trap 15 ions in a chain for the simulation, and the circuits use 4 of those ionic qubits. Before each circuit iteration, ions are cooled using Doppler cooling and Raman sideband cooling, and then reset to the logical  $|0\rangle$  state via optical pumping. The qubit state is manipulated using 355-nm pulsed Raman beams. Single qubit gates are implemented using SK1 pulses [32], and two-qubit gates are mediated by Mølmer-Sørensen interactions [33] —these gates are run sequentially. We measure the qubit states by shining 369-nm light resonant on the  $^2S_{1/2} \rightarrow ^2P_{1/2}$  cycling transition that scatters photons.

The time series data used to construct the NMR spectrum of acetonitrile was collected over the course of 12 days, during which the quantum computer’s hardware remained unchanged. The data consists of a 1000 shots of 102 different circuits, for which 8 different initial states were prepared. While running circuits on the quantum machine, we perform system calibrations of trap voltages and gate amplitudes every hour to mitigate effects of system drift on circuit performance. We do not correct for state preparation and measurement (SPAM) errors in this study, and a table of our system’s SPAM characterization is presented in Ref. [10].

### B. Time-evolution circuit synthesis

We use the numerical optimization algorithm in Ref. [14] to synthesize the circuits implementing the time-evolution unitary  $U(t) = \exp(-iHt/\hbar)$ , with the Hamiltonian given in Eq. (S.1). The algorithm implements a bottom-up approach, building the single- and two-qubit gate decomposition of a  $n$ -qubit unitary by iteratively searching for a  $m$ -qubit gate decomposition with  $m < n$ . Initially,  $m$  is set to  $n - 1$ . The algorithm is hardware topology and gateset aware; to specialize for the trapped-ion system, we allow all-to-all connectivity of qubit interactions and choose Mølmer-Sørensen gates with variable angles as the interaction gate.

We choose a unitary error of  $\epsilon = 10^{-2}$ , with the synthesis algorithm producing a circuit in terms of Mølmer-Sørensen (MS) gates and generic single-qubit rotations that approximates the true time-evolution unitary within this error. We then iteratively perform a X-Z-X decomposition of each single-qubit rotations, commuting the trailing X rotation through each MS gate before decomposing the next single-qubit rotation. This optimization results in roughly two Z rotations and two X rotations after each MS gate. As Z rotations are implemented virtually in the trapped-ion system, the final circuit has only two physical single-qubit rotations for each MS gate, and thus the physical circuit depth is reduced compared to the initial output of the synthesis algorithm. An example of the final optimized circuit is shown in Fig. S1. Typically, the produced circuits were composed of up to 40 MS gates and 80 physical single-qubit gates.

### C. Compressed sensing

A general function in the frequency-domain that is nonzero in a specified frequency window can be reconstructed by Fourier transforming a corresponding time-domain signal that is uniformly sampled at the Nyquist rate. If the function is known to be sparse in the frequency domain, however, the time signal can be undersampled by choosing a non-uniform subset of time points which still capture the relevant information in the frequency domain [21]. The missing points on the original uniform time grid create artifacts in Fourier transform of the signal, however, which must then be removed using a compressed sensing reconstruction algorithm that exploits the assumed sparsity of the frequency signal. NMR spectra are often sparse as they are composed of a series of Lorentzian peaks, and therefore compressed sensing techniques allow for a dramatic reduction in the sampling required during an NMR experiment [13].

This sparsity can also be exploited in quantum simulations of NMR experiments by computing the FID at only the undersampled time points and then reconstructing the spectrum. We compute the FID at 102 out of the  $N_s = 4096$  time points on the uniform grid, choosing the points according to a sine-weighted Poisson gap schedule. Such schedules have been shown to reduce undersampling artifacts [23]. The points are randomly chosen with the likelihood to pick a point  $m + 1$  on the uniform grid, given we have picked a point  $m$ , set by a Poisson distribution with mean proportional

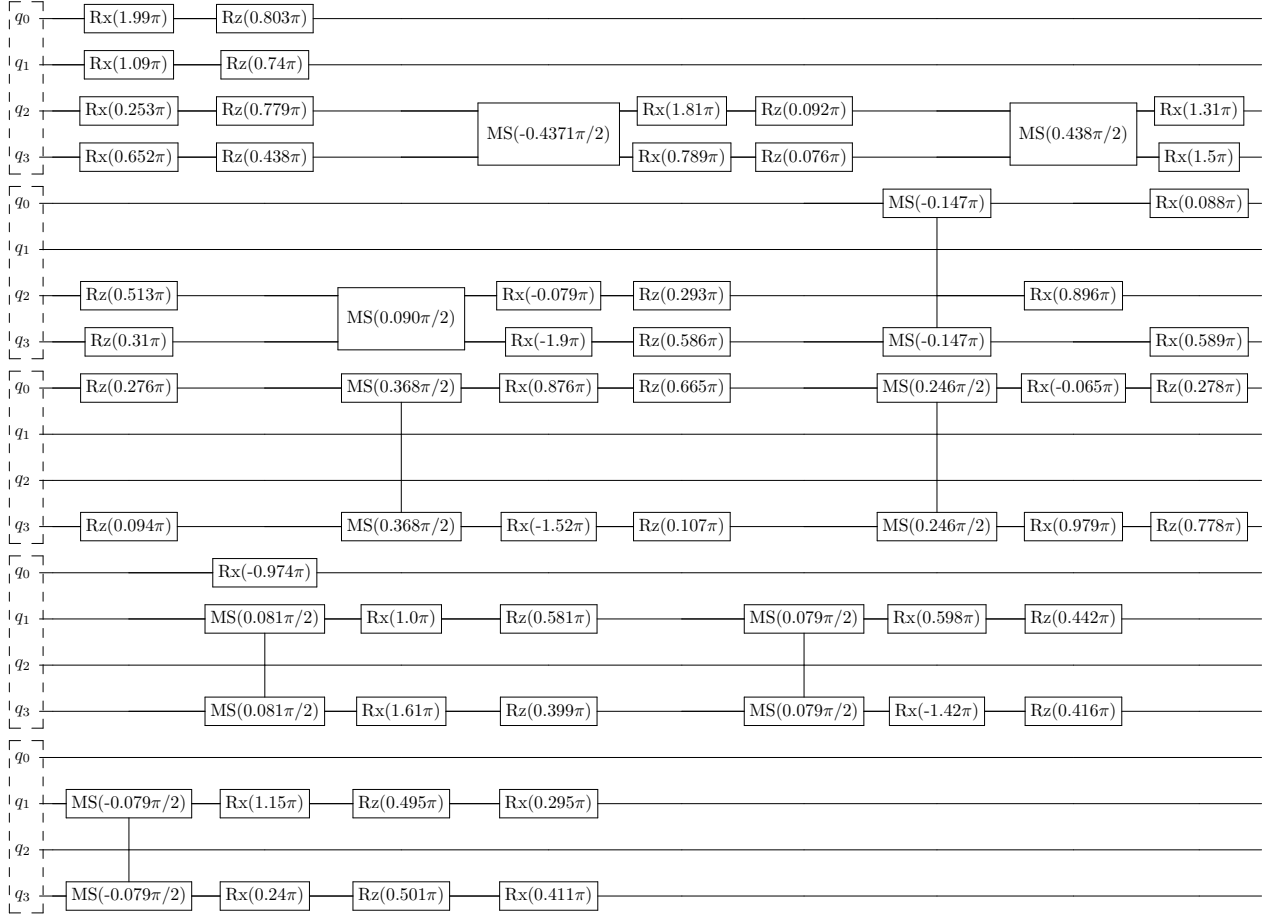


Figure S1: **Time-evolution circuit.** Example time-evolution circuit generated by numerical synthesis algorithm corresponding to  $t = 0.07$  s. Circuit is split into five rows and read top to bottom, with the start of each row indicated by a dashed box around the four qubits in the experiment.

to  $\sin(\alpha\pi m/N_s)$ . Specifically, we choose  $\alpha = 0.5$ , resulting in a schedule that is dense at short times before becoming increasingly sparse at later times. We find that this choice allows for much larger compression compared to a schedule with uniformly distributed gaps between points, or a schedule that is also dense at late times (corresponding to  $\alpha = 1$ ). After computing the undersampled FID, we reconstruct the spectrum using the iterative soft thresholding (IST-S) algorithm [13].

In Fig. S2(a), we plot the FID computed via noisy emulations for all 4096 time points, and compare with the 102 points that were experimentally computed. This plot corresponds to Fig. 2(a) of the Main Text, but with the quantities depicted over the full time grid. In Fig. S2(b), we plot the spectrum computed after padding the experimental data with zeros for all time points that were not computed. We see that there is some signal at the spectral peaks expected from the noisy emulation, but the signal-to-noise is very large. The zero-padded spectrum in this plot corresponds to the green dots in Fig. 2(b) of the Main Text. In Fig. S2(c), we plot the compressed sensing reconstruction of the experimentally computed spectrum, and see that the signal-to-noise is dramatically improved. The reconstructed spectrum in this plot corresponds to the yellow curve in Fig. 2(c) of the Main Text.



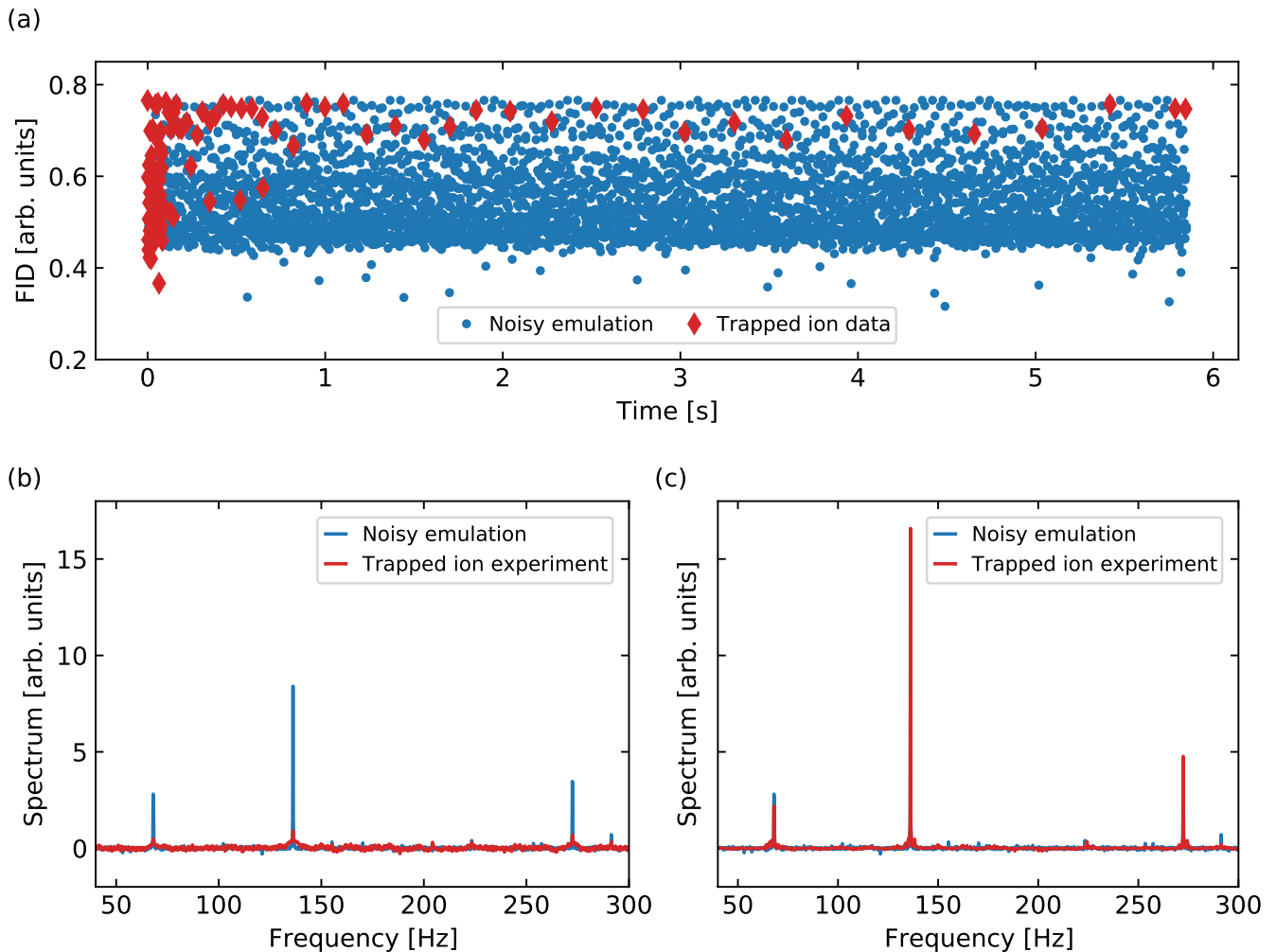


Figure S2: **Compressed sensing reconstruction.** (a) Comparison of the FID for noisy quantum circuit emulation on a fully sampled uniform time grid of 4096 points (blue circles) and the 99 data points experimentally measured on the ion trap device (red diamonds). (b) Fourier transform of the FID after replacing unsampled points with zeros. (c) Reconstructed spectrum after applying the iterative soft thresholding algorithm. The noise is modeled by two-qubit gates subject to both amplitude and phase damping with rates 0.005 and 0.035 respectively.

#### D. Scaling to larger systems

The numerical optimization algorithm we use is likely to be limited to producing time-evolution circuits for systems of up to  $\sim 7$  spins [14]. This tool can still prove useful, however, when scaling to large, classically-intractable NMR simulations by exploiting the cluster structure of these molecules (see Fig. 3A of the Main Text). The strongly-interacting clusters are usually formed from 4-7 spins, and the optimization algorithm can be used to synthesize the time-evolution circuit for each cluster. These circuits can then be combined with a Trotter formula to implement the time-evolution of the entire systems [25]. Compared to a Trotter decomposition of the entire system, such a hybrid approach can reduce the overall circuit depth, as discussed in Sec. S3B. Furthermore, at the level of discretization estimated in Fig. 3 of the Main Text, the simulation times are small enough that the optimization should converge very quickly, potentially enabling real-time compilation of the overall time-evolution circuit.

We note that numerical circuit synthesis of small subsystems and compressed sensing techniques form a synergistic combination of tools. For example, cluster-exploiting Trotter formulas allow for an overall reduction in resource cost at all simulation times, while compressed sensing non-uniform sampling schedules may sample more densely from short times where the resource cost is smallest. On the hardware side, the all-to-all connectivity of trapped ions makes them well-suited to the interaction graphs within clusters, and may allow comparatively smaller gate counts

for the cluster evolution circuits. The relatively slow cycle time of ion devices is ameliorated by compressed sensing techniques, which reduce the number of time points that must be sampled. The combination of numerical circuit synthesis, which exploits the clustered interaction structure of a system, and compressed sensing, which exploits sparsity of the observable of interest in the transform domain, may similarly prove useful for quantum simulations in quantum chemistry and condensed matter systems where both of these characteristics are often present [15].

## S2. SPECTRAL PEAK AT $J/2$

The acetonitrile spectrum we compute on the trapped ion quantum computer, depicted in Fig. 1 of the main text, exhibits a resonance at frequency  $J/2$  which does not appear in the NMR experiment of Ref. [12]. Here, we explain the origin of this additional peak and discuss how to prevent such artifacts from appearing in future experiments.

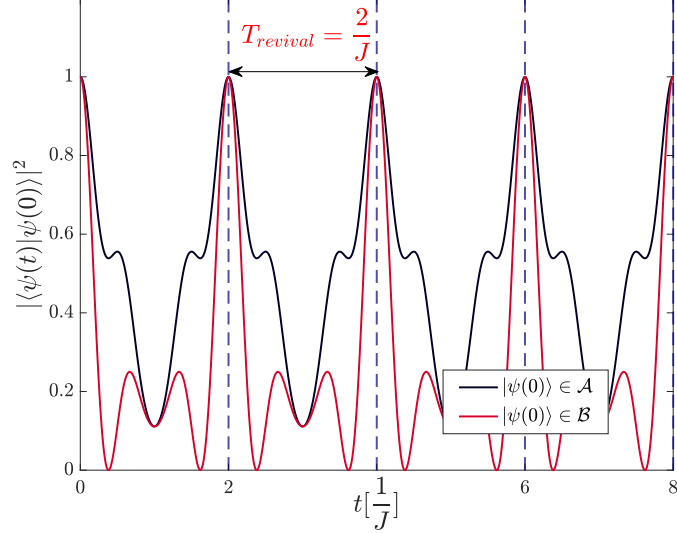


Figure S3: **Magnetization basis state revivals.** A system initialized in state  $|\psi(0)\rangle$  selected from magnetization basis states  $\mathcal{A} = \{\tilde{m}_1, \tilde{m}_3, \tilde{m}_5\}$  and  $\mathcal{B} = \{\tilde{m}_4, \tilde{m}_6, \tilde{m}_8\}$  undergoes revivals with a period  $2/J$ .

The zero-field nuclear spin Hamiltonian of acetonitrile is

$$\hat{H} = J \left( \hat{\mathbf{S}}_1 + \hat{\mathbf{S}}_2 + \hat{\mathbf{S}}_3 \right) \cdot \hat{\mathbf{S}}_4, \quad (\text{S.1})$$

where  $\{\hat{\mathbf{S}}_1, \hat{\mathbf{S}}_2, \hat{\mathbf{S}}_3\}$  represent the three  $^1\text{H}$  and  $\hat{\mathbf{S}}_4$  represents the  $^{13}\text{C}$ . The eight positive magnetization states used to compute the FID, see Eq. (3) of the main text, and their magnetizations are

$ \tilde{m}_1 = 1.626\rangle =  0000\rangle$	$\tilde{m}_1 = 1.626$
$ \tilde{m}_2 = 1.626\rangle =  0001\rangle$	$\tilde{m}_2 = 1.374$
$ \tilde{m}_3 = 1.626\rangle =  0010\rangle$	$\tilde{m}_3 = 0.626$
$ \tilde{m}_4 = 1.626\rangle =  0011\rangle$	$\tilde{m}_4 = 0.374$
$ \tilde{m}_5 = 1.626\rangle =  0100\rangle$	$\tilde{m}_5 = 0.626$
$ \tilde{m}_6 = 1.626\rangle =  0101\rangle$	$\tilde{m}_6 = 0.374$
$ \tilde{m}_7 = 1.626\rangle =  1000\rangle$	$\tilde{m}_7 = 0.626$
$ \tilde{m}_8 = 1.626\rangle =  1001\rangle$	$\tilde{m}_8 = 0.374$

The small, four spin Hilbert space of the NMR active nuclear spins of the molecule along with the molecules highly symmetric nature—as codified by the single interaction scale  $J$  in Eq. (S.1)—combine to yield perfect revivals when the system is prepared in six of the above magnetization basis states. These states can be grouped into the triads  $\mathcal{A} = \{\tilde{m}_1, \tilde{m}_3, \tilde{m}_5\}$  and  $\mathcal{B} = \{\tilde{m}_4, \tilde{m}_6, \tilde{m}_8\}$  and we depict their revivals in Fig. S3. When viewed in the energy eigenstate basis, each of these six magnetization basis states only has weight on energy eigenstates whose eigenvalues are integer multiples of  $J/2$ . Consequently, all energies relevant to the dynamics are commensurate with a smallest

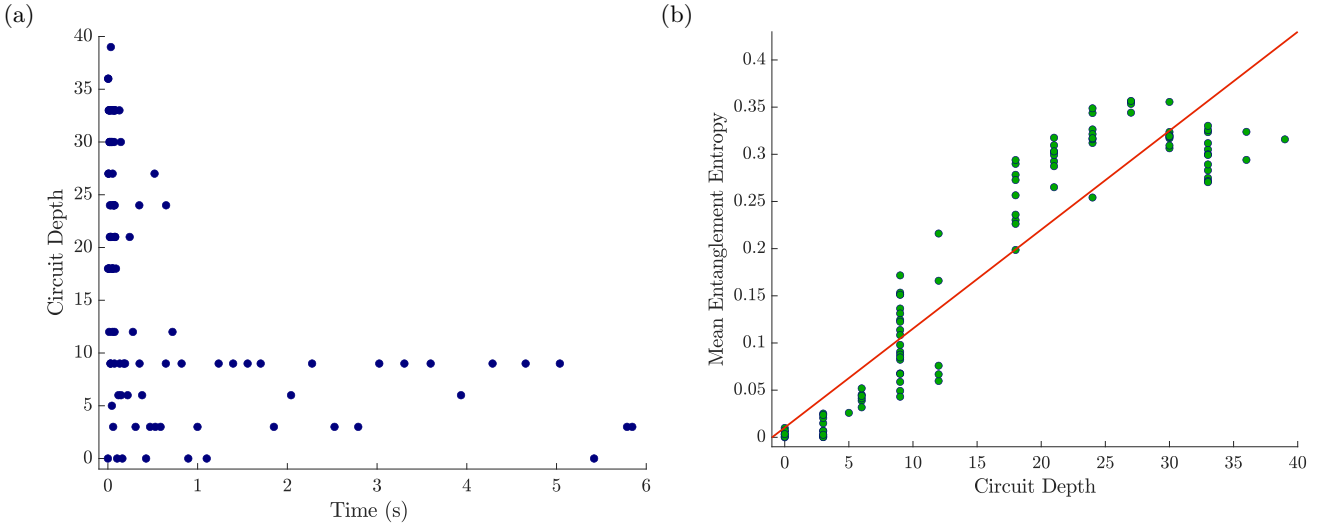


Figure S4: **Synthesized circuit depth and entanglement.** (a) Two-qubit gate count of synthesized time-evolution circuits for each FID evolution time measured on the trapped-ion device. (b) Entanglement entropy of the system at a particular evolution time compared to the two-qubit gate count of the circuit implementing that evolution. We average the final entanglement entropy for systems initialized in each of the eight magnetization basis states used to compute the FID.

splitting of  $J/2$ , which leads to the state reviving with perfect fidelity at this frequency. The revival of each state is mirrored in its entanglement dynamics. Each magnetization state begins in an unentangled product state, non-monotonically accrues entanglement over a period  $T = \frac{2}{J}$ , and then dis-entangles as it returns to the original product state. The high symmetry and small size of the molecule therefore causes the dynamics to defy usual expectations of ergodicity, with the entanglement of a system initially prepared in one of the states in  $\mathcal{A}$  or  $\mathcal{B}$  oscillating at a frequency  $J/2$  instead of growing monotonically in time.

The numerical optimization algorithm, Ref. [14], we use to synthesize time-evolution circuits for each time point reflects this oscillating entanglement in the gate depth of the synthesized circuits. Specifically, times at which the system is more heavily entangled correspond to deeper circuits with a larger number of two-qubit gates, as can be seen in Fig. S4.

Noise in the system affects deeper circuits more than shallower ones, and therefore imprints the  $J/2$  entanglement oscillation onto the experimentally measured observable by lowering the fidelity of the signal at this frequency. We can gain visibility into this process by computing the average Bhattacharyya coefficient (BC) between the measured basis state populations and noiseless emulations of the circuits for each time point. The BC is defined as

$$\text{BC} = 1 - \frac{1}{2} \sum_j \left( \sqrt{p(j)} - \sqrt{q(j)} \right)^2, \quad (\text{S.2})$$

where  $j$  runs over all computational basis states, and  $p(j)$  and  $q(j)$  are the corresponding occupation probabilities, given by the diagonal elements of the density matrix, of the two states being compared. The BC gives a measure of the fidelity of the experimental runs and we plot it for every experimentally measured time point in Fig. S5(a). We see that it varies as a function of time, and these oscillations correspond to time-evolution circuits that have a larger two-qubit gate count as shown in Fig. 2C of the Main Text. In Fig. S5(b), we use the same compressed sensing algorithm used to compute the NMR spectrum to reconstruct the Fourier transform of the BC dynamics depicted in Fig. S5(a). We observe a sharp peak at  $J/2$ , confirming that the fidelity of the experimental oscillates at a frequency of  $J/2$ . These oscillations corresponding to oscillating depths of the synthesized circuits, which in turn reflect the entanglement revivals of the molecule's underlying dynamics. The above story confirms why noisy circuit simulations, such as the one depicted in Fig. 2A of the main text, also exhibit this  $J/2$  resonance peak in the computed NMR spectrum regardless of the type of decoherence channel used to simulate noise.

artifact peaks such as the  $J/2$  resonance can easily be removed in future experiments. By padding all time-evolution circuits so that they have roughly the same depth as the deepest synthesized circuit, the noise in the system can no longer imprint any frequency on the measured signal as the gate depths no longer oscillate. We show in Fig. S6 that such padding dramatically decreases the height of the  $J/2$  peak in noisy circuit simulations of the experiment. The

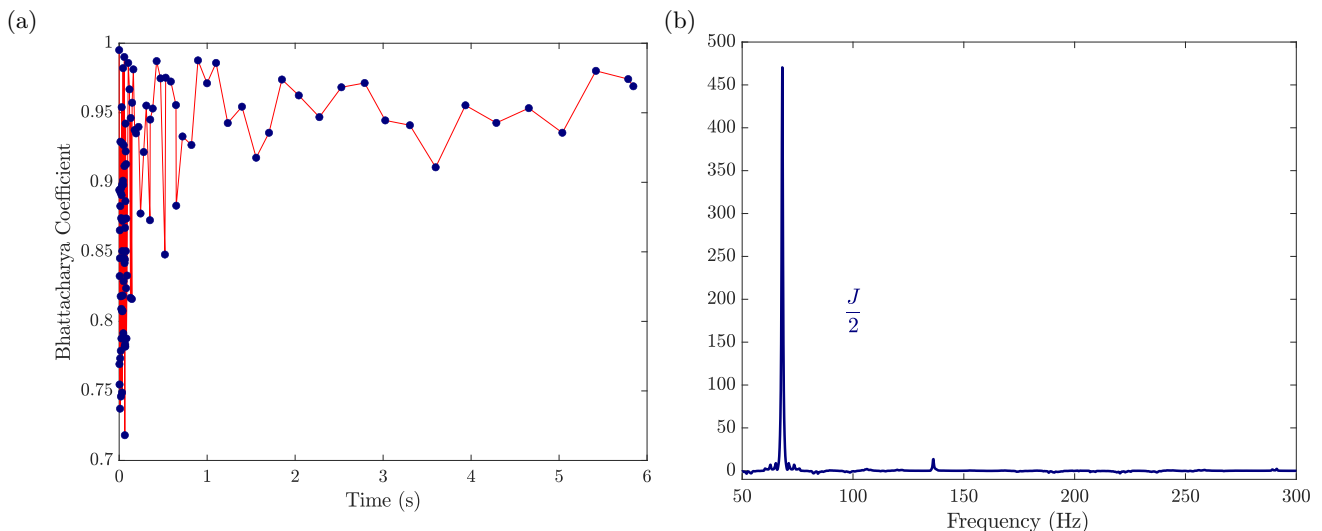


Figure S5: **Bhattacharyya coefficient between trapped ion measurements and noiseless emulation of the experiment.** (a) BC vs evolution time. (b) Compressed sensing reconstruction of the frequency spectrum of the BC. We see that the BC, a measure of the fidelity of the system, only varies at the frequency  $J/2$  with which the system’s entanglement, and therefore circuit depth, oscillates.

padding will, however, slightly decrease the overall fidelity of the computed FID as every point will be subject to as much noise as the deepest time-evolution circuit. If we desire to compute the maximum fidelity signal allowable by hardware, we can compute FID twice - once with padded circuits and once without. Any feature that vanishes in the padded experiment can be removed from the higher fidelity non-padded experiment.

Lastly, we note that artifact peaks are unlikely to appear during quantum simulations of the majority of NMR experiments, and become increasingly unlikely when scaling to classically intractable systems. Small molecules which do not exhibit the high degree of symmetry exhibited in Eq. (S.1) are unlikely to exhibit the dynamical revivals at the heart of artifact peaks. Larger systems, including those with some symmetry, are even less likely to exhibit revivals as entanglement spreads throughout the system. In fact, classically intractable systems are intractable precisely because quantum correlations spread quickly throughout the system. Furthermore, quantum simulation algorithms that generalize to larger systems, such as product formulas, typically have gate depths that monotonically increase with the simulation time. This relationship is also directly true for analog quantum simulation. Noise in these cases will lead only to a broadening of spectral peaks, and cannot imprint any artifact frequencies on the measured signal. Therefore, artifact peaks are unlikely to be a common concern during quantum simulations of NMR experiments. Even in small, highly symmetric systems where the peaks might appear, circuit padding is a cheap way to remove these artifacts.

### S3. RESOURCE ESTIMATES FOR NMR SIMULATION

The standard Hamiltonian simulation task (e.g. by Suzuki-Trotter product formula, hereafter product formula), seeks to approximate exact unitary dynamics within a finite precision  $\epsilon$  (clarified below). However, the spectral resolution—alternatively, the line-width—of NMR experiments are set by the dephasing of the nuclear spins. The inherent dephasing in the experiments we seek to simulate reduces the resource cost simulation compared to purely coherent systems. In what follows, we show how this discrepancy between the standard Hamiltonian simulation task (simulating a unitary to finite *precision*) and the task of employing Hamiltonian simulation as a sub-routine to compute an NMR spectrum (with finite *spectral resolution*) can yield gate counts that are several orders of magnitude smaller for the latter task, making it tractable on NISQ devices. To perform Hamiltonian simulation, we proceed by using a variant of first-order product formula that exploits the clustered structural motif present in many molecules that are classical challenging to simulate. In what follows, we first elucidate the distinction between the standard Hamiltonian simulation task and the task at hand and provide bounds on the requisite two-qubit gate fidelity and gate counts for computing NMR spectra with finite resolution. We round out our discussion by providing commutator bounds relevant to estimating the quantum resources required to simulate the NMR spectra of molecules with a clustered interaction structure.

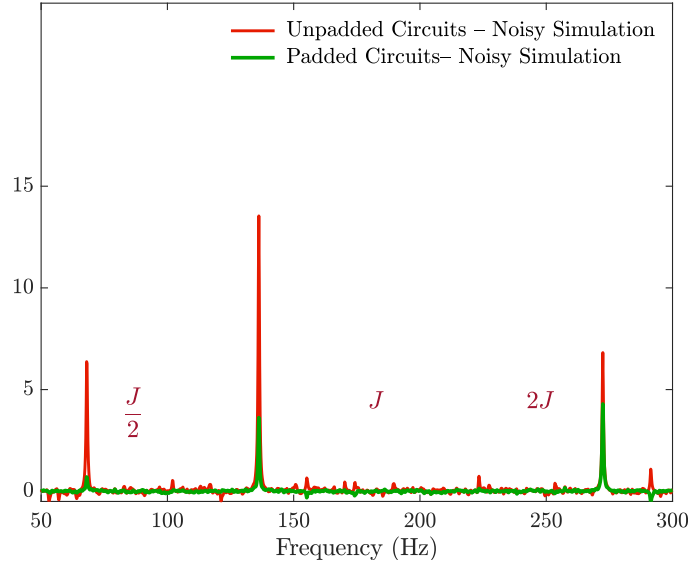


Figure S6: **Noisy circuit simulation.** The zero-field NMR spectrum of acetonitrile computed using noisy circuit simulations with and without padding. The padded circuits no longer have depths that oscillate in accordance with the system’s entanglement, and therefore do not exhibit the artifact peak at  $J/2$ . Noise was simulated by adding a depolarizing channel to each gate, with a rate of  $10^{-3}$  for single-qubit gates and  $10^{-2}$  for two-qubit gates.

### A. Approximating Hamiltonian Dynamics for NMR Simulations

We begin by clarifying the difference between a standard Hamiltonian simulation task and the task of using Hamiltonian simulation to simulate NMR experiments. We consider performing Hamiltonian simulation via first order Trotterization, a simple but powerful and gate efficient method for simulating Hamiltonian dynamics. Keeping our discussion somewhat general for the moment, let’s say we have a Hamiltonian  $H = \sum_{\mu} h_{\mu}$ , composed out of a number of  $N_c$  terms  $h_{\mu}$ . We’d like to replace the time-evolution operator  $U = e^{-i\Delta t H}$ , for some small time-step  $\Delta t$  by our simple product formula:

$$\tilde{U} = \prod_{\mu=1}^{N_c} e^{-i\Delta t h_{\mu}}.$$

It follows from Baker-Campbell-Hausdorff (BCH), by keeping only lowest order contributions in  $\Delta t$ , that

$$\|U - \tilde{U}\| \leq \frac{(\Delta t)^2}{2} \sum_{\mu=1}^{N_c} \left\| \sum_{\nu>\mu} [h_{\nu}, h_{\mu}] \right\|, \quad (\text{S.3})$$

as obtained in Ref. [9]. Consequently, we could also write the fidelity of the simulation as

$$\mathcal{F}_{\delta t} = \|U\tilde{U}\| \geq e^{-\beta(\Delta t)^2/2}, \quad \text{where} \quad \beta = \sum_{\mu=1}^{N_c} \left\| \sum_{\nu>\mu} [h_{\nu}, h_{\mu}] \right\| \quad (\text{S.4})$$

Let’s say we’d like to evolve for a total time  $T = r\Delta t$ , then the total fidelity will be

$$\mathcal{F}_{PF}(T) = \prod_{i=1}^r \mathcal{F}_{\delta t_i} = e^{-r\beta(\delta t)^2/2} = \exp\left(-\frac{\beta T^2}{2r}\right), \quad (\text{S.5})$$

If we want a precision  $\epsilon$ , then we need  $\mathcal{F} = 1 - \epsilon \approx e^{-\epsilon}$ . This sets the Trotter number  $r$  to achieve a precision  $\epsilon$ :

$$r_{\epsilon} = \frac{\beta T^2}{2\epsilon}. \quad (\text{S.6})$$

Achieving this can be quite challenging for even intermediate times, in particular in NISQ settings.

The task of simulating the relevant dynamics corresponding to an NMR experiment does not, however, require the approximation of unitary dynamics generated by the Hamiltonian to finite, time-independent precision  $\epsilon$ . It requires instead the simulation of a spectrum to finite spectral resolution  $\Delta f$ . In an NMR experiment,  $\Delta f \sim \gamma$ , the dephasing rate of a single nuclear spin in experimentally interrogated sample. Thus, the task of simulating an NMR experiment with resolution  $\Delta f$  is equivalent to simulating Hamiltonian dynamics of a sample of  $N$  spins in which each spin decoherences independently with an *effective* dephasing rate  $\gamma = \frac{\Delta f}{2\pi}$ . Such dephasing exponentially degrades the fidelity, vis-a-vis perfect unitary dynamics given by the Hamiltonian, as  $\mathcal{F}_{NMR} \sim e^{-\gamma N t}$ . Thus, there is a subtle but essential distinction between the task of approximating a unitary to multiplicative error  $\epsilon$  and performing Hamiltonian simulation to compute a spectrum with finite spectral resolution  $\Delta f$ . If, for the moment, we neglect decoherence in our quantum hardware and consider only algorithmic error due to our product formula, as given in S.5, then setting  $\mathcal{F}_{PF}(T) = \mathcal{F}_{NMR}(T)$  we find an upper bound for the minimal necessary Trotter number:

$$r_{NMR} = \frac{\beta T}{2\gamma N}. \quad (\text{S.7})$$

As typical experiments interrogate regimes up to where  $\gamma T \sim 1$ , the number of Trotter steps  $r$  is reduced by a factor of  $\frac{N}{\epsilon}$  as compared to the case of fixed precision—for the examples examined in the Main Text, this corresponds to a  $O(10^3 - 10^4)$ -fold decrease in the number of steps required to realize the longest dynamics relevant to experiment.

For a more careful estimate of the necessary resources, we also account for the decrease in fidelity due to decoherence in our quantum hardware. We describe the decaying fidelity of our experiment due to hardware error as  $\mathcal{F}_h(T) \sim F^{r N_g}$ , where  $F$  is the two-qubit gate fidelity,  $r$  is the Trotter number, and  $N_g$  is the number of two-qubit gates required to realize a particular Trotter step. Note that by such a description, we assume that hardware error and algorithmic error are independent of each other and that two-qubit gates dominate the hardware error. The product of  $\mathcal{F}_h(T)$  and  $\mathcal{F}_{PF}T$  must be greater than or equal to  $\mathcal{F}_{NMR}$  in order to perform reliable simulation. We obtain, the following requirement:

$$-N_g \log(F) + \beta(\Delta t)^2/2 \leq \gamma N \Delta t. \quad (\text{S.8})$$

This will have a solution for the Trotter time step  $\Delta t$  as long as

$$F \geq e^{-\gamma N \Delta t / N_g}. \quad (\text{S.9})$$

Requiring our quantum simulation fidelity to match the fidelity of the experiment—thereby recasting S.8 as an equality—and re-arranging, we can establish an equation for  $\gamma \sim \Delta f$ :

$$\gamma = \frac{1}{N} \left( \frac{\Delta t \beta}{2} - \frac{N_g \log(F)}{\Delta t} \right) \quad (\text{S.10})$$

By optimizing over the Trotter step  $\Delta t$ , we can set the ultimate resolution  $\Delta f_{opt}$  of our experiment:

$$\Delta f_{opt} = \frac{\gamma_{opt}}{2\pi} = \frac{1}{2\pi N} \sqrt{2N_g \beta \log(1/F)} \quad (\text{S.11})$$

Note that this optimal resolution is a simple function of the fidelity of the quantum hardware employed, given by  $F$ , and the efficiency of the algorithm used, as encoded by  $\beta$  and  $N_g$ . On the hardware side, improving gates and thereby improving the gate fidelity, parametrized by  $F$ , would lower the resolution. Similarly, on the algorithmic side, finding more efficient circuits to realize a single Trotter step (lowering  $N_g$ ) or better product formulae (lowering  $\beta$ ), would improve the resolution—in what follows, we provide strategies on how to achieve both of these algorithmic improvements.

## B. Commutator Bounds for Clustered Hamiltonians

As implied by Eq. (S.11), decreasing  $\beta$  (defined above in Eq. (S.4)) small would improve the resolution of the simulation. In what follows, we compute  $\beta$ , assuming an NMR Heisenberg Hamiltonian with clustered interactions,

first in the standard way and then by taking advantage of the cluster motif. We show that by doing the latter, we can reduce  $\beta$  substantially.

Before beginning this program, it is useful to establish some intuition for how clustered interactions reduce  $\beta$  vis-a-vis the case of all-to-all couplings. If we take an all-to-all model with some typical coupling  $J/\sqrt{N}$  (taking into account Kac normalization to keep the energy extensive in the system size  $N$ ), we find

$$\beta = O(J^2 N^2), \quad \text{such that} \quad r \sim \left(\frac{JN}{\gamma}\right)^2 (\gamma T). \quad (\text{S.12})$$

The situation changes for clustered Hamiltonians where each spin typically interacts with a sub-extensive number of spins  $k$ . For each term in the latter, only  $k$  terms contribute in the commutator and there are  $kN$  terms, yielding:

$$\beta \sim k^2 N J^2, \quad \text{such that} \quad r \sim \left(\frac{Jk}{\gamma}\right)^2 (\gamma T). \quad (\text{S.13})$$

Note that, due to the clustered nature of the interactions,  $r$  does not scale with  $N$ : Increasing the number of spins does not increase the Trotter number.

Having established a heuristic derivation for the scaling of  $\beta$  and thereby the Trotter number, we turn to the present situation of a Heisenberg model with local fields.

$$H = \sum_{ij} J_{ij} (S_i^x S_j^x + S_i^y S_j^y + S_i^z S_j^z) + \sum_i h_i S_i^z. \quad (\text{S.14})$$

where all terms can be labeled by  $\mu = (i, j, \sigma)$ , indicating the bond and the operator that is acted with. If we perform a scheme which alternates all Ising- $XX$  gates with all Ising- $YY$ 's and all Ising- $ZZ$ 's, then  $\beta$  is comprised of three terms, defined below:  $\beta_1, \beta_2, \beta_3$ .

We first bound  $\beta_1$ , given by:

$$\beta_1 = \sum_{ij} |J_{ij}| \left\| \sum_{kl} J_{kl} [S_k^y S_l^y + S_k^x S_l^x, S_i^z S_j^z] \right\|, \quad (\text{S.15})$$

Straightforward algebra brings us to

$$\beta_1 = \sum_{ij} |J_{ij}| \left\| \sum_k (2J_{ki} (S_k^x S_i^y - S_k^y S_i^x) S_j^z + 2J_{kj} (S_k^x S_j^y - S_k^y S_j^x) S_i^z) \right\|. \quad (\text{S.16})$$

where the fact that  $J_{ij} = J_{ji}$  is used. We therefore have:

$$\beta_1 \leq \sum_{ij} 2|J_{ij}| \sum_k (\|J_{ki} (S_k^x S_i^y - S_k^y S_i^x) S_j^z + J_{kj} (S_k^x S_j^y - S_k^y S_j^x) S_i^z\|), \quad (\text{S.17})$$

which can again be bounded as:

$$\beta_1 \leq 2 \sum_{ij} |J_{ij}| \sum_k |J_{ki}| \| (S_k^x S_i^y - S_k^y S_i^x) S_j^z \| + |J_{kj}| \| (S_k^x S_j^y - S_k^y S_j^x) S_i^z \|. \quad (\text{S.18})$$

Computing the norm directly— $\|(S_k^x S_i^y - S_k^y S_i^x) S_j^z\| = 1/4$ —we arrive at:

$$\beta_1 \leq \sum_{ijk} |J_{ik}| |J_{ki}| \quad (\text{S.19})$$

We can similarly bound  $\beta_2$ , which is given by:

$$\beta_2 = \sum_{ij} |J_{ij}| \left\| \sum_{kl} J_{kl} [S_k^y S_l^y, S_i^x S_j^x] \right\|, \quad (\text{S.20})$$

as

$$\beta_2 \leq \frac{1}{2} \sum_{ijk} |J_{ik}| |J_{kj}| \quad (\text{S.21})$$

Finally there are local field terms, which if we do them together with the ZZ gates would give

$$\beta_3 = \sum_i |h_i| \left\| \sum_{kl} J_{kl} [S_k^y S_l^y + S_k^x S_l^x, S_i^z] \right\|, \quad (\text{S.22})$$

which gives

$$\beta_3 = 2 \sum_i |h_i| \left\| \sum_k J_{ki} (S_k^x S_i^y - S_k^y S_i^x) \right\|, \quad (\text{S.23})$$

and thus

$$\beta_3 \leq \sum_{ij} |h_i| |J_{i,j}| \quad (\text{S.24})$$

However, one can obtain a tighter bound by treating the Z-gates as a single global gate. Doing so yields:

$$\tilde{\beta}_3 = \left\| \sum_{kl} J_{kl} [S_k^y S_l^y + S_k^x S_l^x, \sum_i h_i S_i^z] \right\|, \quad (\text{S.25})$$

in which case we'd arrive at

$$\tilde{\beta}_3 \leq \frac{1}{2} \sum_{ij} |h_i - h_j| |J_{i,j}| \leq \beta_3. \quad (\text{S.26})$$

Therefore, we have that the total spectral norm of the nested commutator  $\beta$  is bounded by:

$$\beta \leq \beta_1 + \beta_2 + \tilde{\beta}_3 \leq \frac{3}{2} \sum_{ijk} |J_{ik}| |J_{kj}| + \frac{1}{2} \sum_{ij} |h_i - h_j| |J_{i,j}|. \quad (\text{S.27})$$

For many molecules, the interactions between nuclear spins follows a clustered motif. In particular, we examine the computational resources to simulate classically hard molecules that are composed of strongly-interacting clusters tethered together with weakly interacting links. We leverage the clustered motif by performing a variant of first-order Trotter formula wherein the dynamics of the small clusters are numerically synthesized to high precision, using for example the algorithm of Ref. [14], while weak interactions between such clusters are rendered via a pairwise Trotter decomposition of the Hamiltonian.

To understand how this modifies  $\beta$ , we consider the following Hamiltonian:

$$H = H_c + \sum_{i,j} J_{i,j} (S_i^x S_j^{x,c} + S_i^y S_j^{y,c} + S_i^z S_j^{z,c}) + \sum_i h_i S_i^z, \quad (\text{S.28})$$

and

$$H_c = \sum_{k,l} V_{k,l} (S_k^{x,c} S_k^{x,c} + S_k^{y,c} S_l^{y,c} + S_k^{z,c} S_l^{z,c}) + \sum_k h_k S_k^{z,c}, \quad (\text{S.29})$$

where the superscript simply indicates that the operator belongs to the cluster  $H_c$ . If we could synthesize the Hamiltonian of the cluster efficiently (see below), we find:

$$\beta \leq \frac{3}{2} \sum_{i,j,k} |J_{i,k} V_{k,j}| + \frac{3}{2} \sum_{i,j,k} |J_{i,k} J_{k,j}| + \frac{1}{2} \sum_{i,k} |J_{i,k}| |h_k - h_i|. \quad (\text{S.30})$$

By comparing Eq. (S.30) with Eq. (S.27), we see that the latter avoids terms with intra-cluster couplings (i.e. terms like  $V_{i,j} V_{k,l}$ ). For the cases considered in the Main Text, making use of the cluster structure in this manner reduces the Trotter number by one to two orders of magnitude.